

Fast neutron forward distributions from C, Be, and U thick targets bombarded by deuteronsS. Ménard,¹ M. Mirea,² F. Clapier,¹ N. Pauwels,¹ J. Proust,¹ C. Donzaud,¹ D. Guillemaud-Mueller,¹ I. Lhenry,¹A. C. Mueller,¹ J. A. Scarpaci,¹ and O. Sorlin¹¹*Institut de Physique Nucléaire, Orsay 91406, France*²*Institute of Physics and Nuclear Engineering, P.O. Box MG-6, Bucarest, Romania*

(Received 14 December 1998; published 9 March 1999)

Measured angular and energetic distributions of neutrons obtained by bombarding Be, C, and U thick targets with ^2H at 17, 20, and 28 MeV incident energies are reported. The data were obtained using the time-of-flight method. The energetic distributions of neutrons were determined at 0° , 5° , 10° , and 20° . The data are compared with a modelization based on stripping formalism extended for thick targets. [S1098-4402(99)00029-4]

PACS numbers: 28.20.-v, 29.25.Dz, 25.85.Ec

I. INTRODUCTION

In principle, to produce neutron rich radioactive beams with sufficient intensities, a source of isotopes far from the valley of β stability can be obtained through the fission of ^{238}U induced by fast neutrons [1,2]. A very promising way to assess the feasibility of these very intense neutron beams is to break an intense ^2H beam in a dedicated converter. The main objective of the SPIRAL and PARRNE (Production d'Atomes Radioactifs Riches en Neutrons) R&D projects is the investigation of the optimum parameters for a neutron rich isotope source in accordance with the scheme presented above. In such conditions, the charge particle energy loss can prevent the destruction of the fission target. In the frame of these projects, special attention is dedicated to the energetic and angular distributions of the neutrons emerging from a set of converters at a series of ^2H incident energies. Deuteron beams at energies less than 30 MeV are particularly interesting because it is expected that, after the disintegration in the ^{238}U target, the neutron rich radioactive fission products are cold enough, thus avoiding the evaporation of a too large number of neutrons [3]. Unfortunately, at smaller incident energies, the angular distribution becomes broader and, if the converter is far from the neutron rich isotope ^{238}U source, only a relatively small number of neutrons can be collected to induce fission reactions. For such purposes, one needs experimental angular distributions at given energies for different types of converters and to elaborate a theoretical tool in order to estimate accurately the characteristics of the secondary neutron beam. In this paper, the experimental results were obtained with 17, 20, and 28 MeV deuteron energies on Be, C, and U converters using the time-of-flight (TOF) method. These data are compared to results given by a model valid at higher energy in order to obtain pertinent simulations in a large range of incident energies [4]. Many theoretical tools were developed to characterize the properties of the neutron beams emerging from thick targets. In many of these treatments the target is divided into circular slices with uniform or energy dependent thick-

nesses [5,6]. The Serber formalism is used to compute the angular and energetic distribution in each of these slices [4]. The final distribution is obtained by superposing the partial yields with some weights. Other contributions consider that a polynomial fit [7] can give sufficient information about the neutronic distributions for a specific setup. In this contribution, the Serber model, considered with its improvements which account for the Coulomb deflection and the mean straggling of the beam in the material, is compared to experimental data in order to verify the validity of this alternative theoretical method for the characterization of the emerging neutron flux. This formalism hereafter can only be applied to fast neutron yields.

II. EXPERIMENTAL SETUP

The measurements of the angular and energetic distributions of different targets were performed with the classic TOF technique [8]. The DEMON-type detectors (filled with NE213 organic scintillator liquid) are described elsewhere [9]. The scintillator cells have a cylindrical shape with a 16 cm diameter and a 20 cm length. The threshold of each detector was determined with a Co source. The values are presented in Table I in relation to the angle of detection (0° means beam direction) and in connection with the light output signal in electron-equivalent energy. The DEMON detector efficiency is known for a threshold of 1.9 MeV [9], and the neutron energy dependence of the efficiency on the threshold also exists. The experimental data are reported, as in

TABLE I. Experimentally determined thresholds for the detectors disposed at the four different angles.

Angle ($^\circ$)	Threshold (keV)	Neutron threshold (MeV)
0	430	1.5
5	513	1.9
10	750	2.5
20	430	1.5

other publications, above 4 MeV because the systematic errors obtained at lower neutron energies are too large. The flight distance between the target and our detectors was fixed at 4 m. The neutron flux was corrected for attenuation in air. The energetic resolution for 30 MeV nucleons was 10%. The pulsed ^2H beam at a frequency of 1.25 MHz was delivered by the Tandem accelerator at IPN Orsay (width at half maximum of the pulse 1–2 ns associated with a hf signal). The intensity was between 30 and 150 pA.

The targets were chosen in such a way that thicknesses correspond exactly to the range of deuterons up to twice the range of deuterons for an ^2H incident energy of 30 MeV: the thicknesses were 3, 5, and 1 mm for Be, C, and U, respectively. On the beam line, a 14.2 mg/cm² kapton window (composition: 72% C, 2.7% H, 7.6% N, and 17.5% O) causes a projectile energy loss of 0.688, 0.601, and 0.455 MeV for the incident energies of 17, 20, and 28 MeV, respectively. The Serber mechanism predicts similar proton and neutron yields with a most probable energy approaching half of the initial energy of the beam. The protons were attenuated in the target and in the air. With the detectors being placed at a distance of 4 m from the target, only protons with more than 20 MeV can reach them (the maximum most probable energy of the protons in this work being 14 MeV). Moreover, the window of the detectors can also stop charged particles, so that their detection is unlikely. The targets were also surrounded with a plasticized Al envelope (for protection purposes) of 0.1 mm thickness. The experimental setup is presented in Fig. 1.

The kapton window and the plasticized Al foil create some neutrons which overlap the yields emerging from our targets. This effect corrupted our experimental data only to a small extent, the kapton and Al pieces being very thin. A correction of the experimental data by eliminating the events emerging from these thin foils is not possible for our targets. So, it can be considered that the experimental distributions are obtained from the incident energies of deuterons 28, 20, and 17 MeV.

The errors on the experimental data are roughly $\pm 15\%$ and will not be plotted on the figures to avoid confusion.

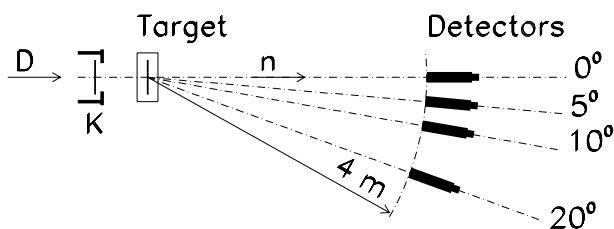


FIG. 1. Experimental setup. D represents the deuteron beam, n the emerging neutrons, and K is the kapton window. The target is surrounded by the plasticized Al foil and the detectors are disposed at 4 m from the target.

III. FORMALISM

At first instance, the formulas are derived for Be targets. The main extension of the Serber formalism is given by effecting averages over the thickness of the target and over selected angles. In the case of thick targets, the thickness will always be considered as equal to the range of the ^2H as a function of its incident energy in the given material. The generalization is described in Sec. IV. The angular distribution $P_s(\theta)$ is determined rigorously in Ref. [4] using the hypothesis of a transparent nucleus. The choice of this hypothesis was decided by the fact that the experimental angular distributions for Be and U [4,10] (at an incident energy of the deuterons of 190 MeV) are better reproduced by the transparent nucleus than by the opaque one. The angular distribution is thus

$$P_s(\xi) = G \left(\frac{u^{3/2} P_{1/2}(u)}{2\pi(1 + \xi^2 + \xi_c^2)^{3/2}} \right), \quad (1)$$

which is equivalent to

$$P_s(\theta) = P_s \left(\xi = \frac{\theta}{\theta_0} \right) \theta_0^2, \quad (2)$$

where θ is the angle of detection in the laboratory frame. Here G is an operator which has the effect of spreading the angular distribution by an additional Gaussian distribution,

$$G = \exp \left\{ \frac{\xi_s^2 t}{4T} \Delta \right\}, \quad (3)$$

due to the multiple scattering of the primary beam in the target material, the so-called angular straggling. In the third-order approximation, this operator averaged over the thickness can be written as

$$G = 1 + \frac{\xi_s^2 \Delta}{8} + \frac{\xi_s^4 \Delta^2}{96} + \frac{\xi_s^6 \Delta^3}{864}, \quad (4)$$

Δ having a θ dependence in polar coordinates,

$$\Delta = \frac{1}{\xi} \frac{\partial}{\partial \xi} \xi \frac{\partial}{\partial \xi}. \quad (5)$$

In the above formulas we used normalized angles $\xi = \theta/\theta_0$, $\xi_s = \theta_s/\theta_0$, and $\xi_c = \theta_c/\theta_0$. θ_0 represents the mean angle of deflection solely due to the breakup reaction of the deuteron,

$$\theta_0 = \arctan \left[\left(\frac{\epsilon_d}{E_d} \right)^{1/2} \frac{1}{1 - \frac{E_d}{Mc^2}} \right], \quad (6)$$

with ϵ_d being the binding energy of the deuteron, E_d denoting its incident energy, and M the nucleon mass. θ_c is the angle of deflection of the deuteron in the Coulomb field of the target nucleus,

$$\theta_c = \frac{1}{2} \arctan \left(\frac{E_c}{E_d} \right), \quad (7)$$

where E_b is the Coulomb barrier height,

$$E_c = \frac{Z_t e^2}{r_0 (A_d^{1/3} + A_t^{1/3})}, \quad (8)$$

with the reduced radius $r_0 = 1.2$ fm, A_t, Z_t the mass and atomic number of the target, and A_d the mass number of the deuteron. Finally, θ_s takes into account the spread of the distribution due to the multiple scattering within the target and it is a function of the target thickness. $P_{1/2}(u)$ is the Legendre function

$$P_{1/2}(u) = 1 + \sum_{n=1}^{\infty} (-1)^{n-1} a_n \left(\frac{u-1}{2} \right)^n, \quad (9)$$

$$a_{n+1} = \frac{(2n-1)(2n+3)}{4(n+1)^2} a_n,$$

with the argument

$$u = \frac{1 + \xi^2 + \xi_c^2}{[(1 + \xi^2 + \xi_c^2)^2 - 4\xi^2 \xi_c^2]^{1/2}}. \quad (10)$$

Values of θ_s are also given in Ref. [10] where the Serber theory was applied for the first time.

Finally, an average over the range T of the incident particles in the target weighted by the cross section of the stripping reaction $\sigma(E_d)$ will give the distribution

$$P(\theta) = k_n \frac{\int_0^T \sigma(E_d[t]) P_s(\theta) dt}{\int_0^T \sigma(E_d[t]) dt}, \quad (11)$$

where k_n is a normalization constant which ensures the condition $\int_0^\pi P(\theta) d\theta = 1$, and this formula takes into account the dependence of the cross section $\sigma(E_d[t])$ versus the energy of the deuteron at the depth t . A relation for the cross section will be proposed below.

The parametrization of the angular distribution given by Eq. (1) was chosen because the attempts realized with the second-order approximation in ξ of this equation as indicated in Ref. [4] failed. The second-order approximation in ξ works well only for very small values of θ_0, θ_c , and θ_s , that means for thin targets at high incident energies. The relations used in the computing code are presented in the appendix.

The angular distributions in the frame of this extended Serber model are compared to experimental data for ${}^2\text{H}$ at 16 MeV deuteron incident energy on Be obtained from Ref. [11] and are shown in Fig. 2. The experimental values show that the angular distribution presents a long tail at large angles. This behavior cannot be explained in the frame of the theory if the stripped neutrons alone are taken into account. Serber affirmed that another process (neglected in many publications) can compete to produce neutrons: the direct collision between one of the particles of the deuteron and one nuclear particle of the target. Moreover, he supposed that the number of neutrons produced by each of these two processes are of the same order of magnitude. He expected that almost 10% of the neutrons obtained at 0° at an incident energy of 180 MeV

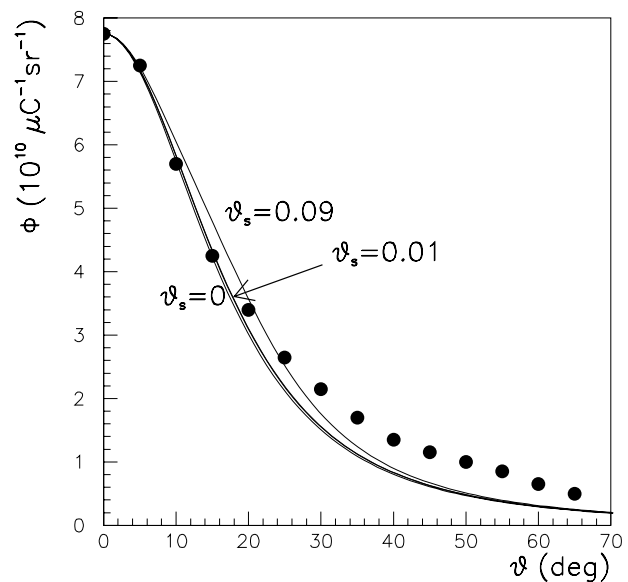


FIG. 2. Comparison between experimental data (from Ref. [11]) obtained for a thick Be target at 16 MeV incident energy (filled circles) and the angular distributions theoretically obtained within the Serber model with and without taking into consideration the straggling: the two curves with $\theta_s = 0.01$ and 0.09 rad. The experimental spectrum is reproduced by the curve with $\theta_s = 0.01$ rad only up to $\theta = 15$. It is clear that, even for larger values of θ_s , the experimental spectra cannot be explained by taking into consideration only the stripped neutrons.

are due to this second process. In fact, as evidenced in Ref. [12], three processes are responsible for the neutron production: stripping of the deuteron, direct interaction producing a neutron recoil, and evaporation. From our comparison, as displayed in Fig. 2, it becomes obvious that at least the second distribution of neutrons must be taken into consideration to reproduce the data and, for simplicity, we chose that given by direct interactions, for which the angular distribution is spread with an angle

$$\theta'_0 = \arctan\left(\frac{E_F}{E_d}\right) \quad (12)$$

instead of θ_0 previously defined, where E_F is the Fermi energy and is approximately 20 MeV. The mathematical formalism remains unchanged. The influence of this new distribution will be analyzed in the following section.

The straggling angle for thin targets can be obtained in the framework of Moliere's theory [13],

$$\theta_s^2 = 0.157 \frac{Z_t(Z_t + 1)z_d^2}{A_t} \frac{T}{E_d^2} B, \quad (13)$$

where B is a coefficient which takes values between 10 and 16, T is the thickness of the target in mg/cm^2 , E_d is taken in MeV, Z_t and A_t address the target nucleus, and $z_d = 1$ is the deuteron charge. For an incident particle of charge 1, values of B are tabulated [14] for different Z_t and T up to $1 \text{ mg}/\text{cm}^2$, this last value of the thickness also reflecting the limit of reliability of the Moliere's

formula. In the case of our targets, the thickness can be considered as equal to the range of the deuterons at the incident energy considered. The neutron cross section decreases dramatically for small values of the deuteron energy. That means that the production of neutrons after the passage of 1 mg/cm² of matter is very small compared to that obtained in the range 0–1 mg/cm². So the straggling associated with the nucleons produced after a 1 mg/cm² passage in matter can be neglected. The mean value of the straggling associated to the neutrons is obtained by averaging the values obtained at three different thicknesses: 0 mg/cm² (θ_s is obviously zero in this case), half-range of ²He in the target, and 1 mg/cm², weighted with their respective cross sections. For Be ($Z_t = 4$ and $A_t = 9$), we obtained approximately $\theta_s = 0.04, 0.05,$ and 0.06 rad for the values of the straggling angle for $E_d = 50, 33,$ and 16 MeV, respectively. These values will represent the starting point in our attempt to fit the experimental angular distribution for Be targets.

Energetic distributions can be approximately determined in the frame of the model. Let us suppose that the deuteron is slowed down in the Coulomb field of the target nucleus and that the Rutherford formula is valid. In this case, the breakup distance of the deuteron ρ_{break} between the centers of the ²H nucleus and the target nucleus can be estimated as follows:

$$\rho_{\text{break}} = \frac{2Ze^2}{E'_d} \left(\frac{1}{\sin(\frac{\theta}{4})} + 1 \right), \quad (14)$$

$$D_1(E, E_d, \theta) = K_1 \frac{1}{\theta_2 - \theta_1} \int_{\theta_2}^{\theta_1} \frac{(\epsilon_d E_d)^{1/2}}{\pi \{ [E - (E_n(\theta_i) + \frac{1}{2}\epsilon_d)]^2 + \epsilon_d E_d \}} d\theta_i, \quad (16)$$

where K_1 is the normalization constant and θ_i is the angle of integration included in the interval $[\theta_2, \theta_1]$. The condition $D_1(E > 2E_d) = 0$ is imposed because neutrons with energy much greater than the incident energy of the deuteron are not expected; in addition, $D_1(E_n < 0) = 0$. Up to now, only the reaction ⁹Be(d, n)¹⁰B ($Q = 4.4$ MeV), which produces the stripped neutrons, was treated. As mentioned above, another kind of process can yield neutrons: the direct nucleon-nucleon collisions. In this case, the following reaction channels can coexist: ⁹Be($d, 2n$)⁹B ($Q = -4.1$ MeV), ⁹Be(d, pn)⁹Be ($Q = -2.2$ MeV), ⁹Be($d, p2n$)²⁴He ($Q = -3.8$ MeV) [15]. In all these channels, the Q value is negative and, therefore, the process is exoenergetic. The neutron can range an amount of energy due to the nuclear process itself. This quantity was appreciated to be $\bar{Q} = 1$ MeV. However, the results of the simulations have a very poor dependence on \bar{Q} if this value varies between 1 and 3 MeV. The distribution for the second process becomes

$$D_2(E, E_d, \theta) = K_2 \frac{(E_F E_d)^{1/2}}{\pi \{ [E - (E_n^{\text{max}} - \frac{1}{2}\bar{Q})]^2 + E_F E_d \}}, \quad (17)$$

where we replaced $\frac{\theta}{4}$ instead of $\frac{\theta}{2}$, considering that once the breakup of the ²H is produced, the neutron is no longer deviated. Because the ²H mass is small in comparison with that of the target nucleus, it can be considered that the angle in the laboratory frame is approximately equal to that in the center-of-mass system. If the breakup is produced at the distance ρ_{break} between the two nuclei, the most probable energy of the emerging nucleon will be

$$E_n(\theta) = \frac{E_d - \frac{Ze^2}{\rho_{\text{break}}(\theta)}}{2}. \quad (15)$$

The most probable energy is denoted E_n in this section, while E is the energy of the neutron given by the theoretical distribution. In the next section and in the following figures, E_n will address the energy of the nucleon in the laboratory frame. Also, it can be considered that the stripping of the proton is produced into a small range $[R_d + R_t, R_t - R_d]$ (where $R_d = 1.2A_d^{1/3}$ fm and $R_t = 1.2A_t^{1/3}$ fm, approximately the radii of the deuteron and of the target nuclei, respectively) of the distances between the centers of the fragments. From Eq. (14), this interval can be associated to an angular one $[\theta_1, \theta_2]$, and the energy distribution will be shifted to smaller values. As pointed out in Ref. [5], the deuteron energy also decreases by an amount equal to the binding energy ϵ_d . So, at an angle θ , the Serber distribution for the first process in the function of the energy E of the neutron (stripped neutron only for the incident energy of the deuteron E_d) appears as

where K_2 is the normalization constant, and this time the reaction takes place after surpassing the Coulomb barrier (the proton must reach the surface of the nucleus) so that the energy of the neutrons becomes

$$E_n^{\text{max}} = \frac{E_d - \frac{Ze^2}{R_t}}{2}. \quad (18)$$

It is considered, too, that $D_2(E > E_d + E_F) = 0$. Furthermore, the parameter θ_s approximately determined previously characterizes the angular straggling which can be associated to an angular spread in the energetic distribution. Moreover, the energy and, therefore, the cross section of the ²H vary within the target at a given depth t . It follows that, on average, the neutrons are emitted in the following distribution:

$$D(E, \theta) = N(\theta) \int_0^T \sigma(E_d[t] dt) \times \int_0^\pi [D_2(E, E_d, \theta_2) + r(\theta_2)D_1(E, E_d, \theta_2)] \times \exp\left(-\frac{(\theta_2 - \theta)^2}{2\theta_s^2}\right) d\theta_2, \quad (19)$$

where $r(\theta_2)$ depends on the emission angle of the neutron. Here $\sigma(E_d[t])$ is the cross section which depends on the energy and, therefore, on the depth in the target t , T is the range in the target corresponding to the incident beam energy, and $r(\theta_2)$ is the ratio at angle θ_2 between the neutrons obtained in the stripping process over those obtained in nucleon-nucleon direct interactions. The normalization constant is obtained as follows:

$$N(\theta) = \frac{\int_{E_{\min}}^{E_{\max}} D(E, \theta) dE}{P(\theta)}, \quad (20)$$

E^{\min} is 4 MeV (it depends on the experimental threshold), while E^{\max} is the incident energy of the primary beam. All the integrations are performed numerically by means of a Gauss-Legendre quadrature in 32 points.

An experimental systematic of yields at 0° exists for thick Be targets bombarded by ^2H at diverse incident energies. From different parametrizations, a good choice is to estimate the yield in the beam direction up to 15 MeV with the formula [16]

$$Y(\theta = 0^\circ)/Q = 10.1 \times 10^{12} (E_d/\text{MeV})^{2.95} \text{ sr}^{-1} \text{ C}^{-1}, \quad (21)$$

and above 15 MeV (up to 50 MeV) with the relation [15]

$$Y(\theta = 0^\circ)/Q = 3.4 \times 10^{13} (E_d/\text{MeV})^{2.5} \text{ sr}^{-1} \text{ C}^{-1}, \quad (22)$$

where Y/Q represents the number of neutrons over the incident charge unit (C). These relations allow the determination of the neutron flux at 0° . This value of the yield furthermore determines the angular distribution quantitatively by means of Eq. (1). Finally, from (19), the energetic distributions could be found for each angle if the ratio between the number of neutrons obtained by stripping and direct nucleon-nucleon reactions is given. Predictions for C and U targets will be obtained by interpolations using the atomic and mass numbers. Also, the experimental systematic of yields for (d, n) reactions in different materials from Ref. [17] can be invoked to predict productions for other kinds of targets by renormalization.

One choice for the dependence of the cross section for a Be target is given by the formula [6]

$$\sigma(E_d) = 0.18 \ln(E_d) + 0.007 E_d \quad (23)$$

and is expressed in b/sr while E_d is in MeV. This relation is determined from experimental data obtained up to $E_d = 15$ MeV and was extrapolated in calculations made in Ref. [6] up to 40 MeV. From our simulations made at 50 MeV deuteron energies, we are able to assess that this relation underestimates the cross sections for deuteron energies greater than 20 MeV.

The next semiempirical formula is proposed to simulate better the behavior of the dependence of the cross section

versus E_d in a larger range of energies

$$\sigma(E_d) = 2. \times 10^{-4} E_d^{1.5} \left| \frac{dE_d}{dt} \right|, \quad (24)$$

where $\frac{dE}{dt}$ is the stopping power in MeV g/cm^2 . This formula is based on Eq. (22) and is valuable for energies greater than 15 MeV. The cross section must be further corrected by the factor $1 - E_c/E_d$, which takes into account the deviation of the trajectory in the Coulomb field. An extrapolation of the formula (24) will be used to determine the yields at 0° for other kinds of targets.

IV. RESULTS AND DISCUSSION

Figure 3 was obtained by summing the two contributions of the stripping reactions and that given by direct nuclear encounters. We have fitted the values of R (the ratio between the total number of neutrons obtained by stripping and the total number of neutrons obtained by direct nuclear encounters), θ_s being determined theoretically, to reproduce as much as possible the experimental data. The quantity R must not be confused with $r(\theta)$, which is the ratio emerging from the two processes at an angle θ . It is evident that the next relation exists between these two quantities

$$r(\theta) = R \frac{P^{\text{stripping}}(\theta) \arctan\left(\frac{1}{2} \left[\frac{E_d}{E_F} \right]^{1/2}\right)}{P^{\text{direct}}(\theta) \arctan\left(\frac{1}{2} \left[\frac{E_d}{\epsilon_d} \right]^{1/2}\right)} \left(\frac{E_F}{\epsilon_d} \right)^{1/2}, \quad (25)$$

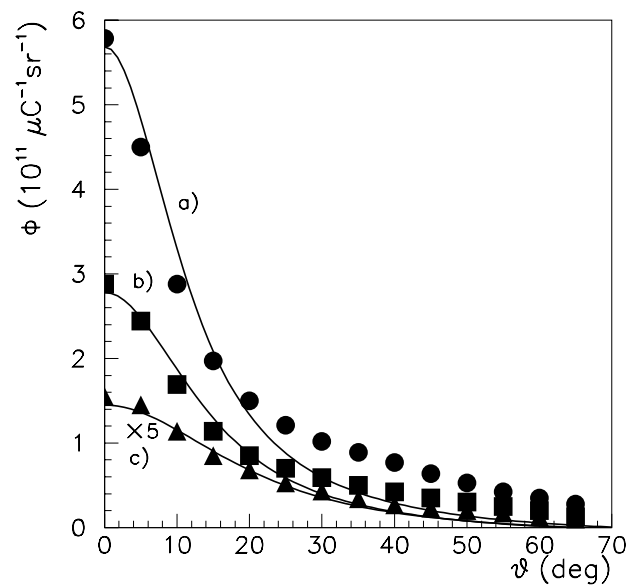


FIG. 3. Comparison between experimental data obtained for Be targets at 50 MeV incident energy (filled circles), 33 MeV incident energy (filled squares), and 16 MeV incident energy (filled triangles) (from Ref. [11]) and results obtained by taking into account the stripping reaction and the direct collisions. Curve (a) is obtained for an incident energy of 50 MeV, $\theta_s = 0.04$ rad, and a ratio $R = 3.7$ between the neutrons considered to originate from the stripping reaction and by direct nuclear encounter. Curve (b) is obtained for an incident energy of 33 MeV, $\theta_s = 0.05$ rad, and $R = 4$. Curve (c) is obtained for an incident energy of 16 MeV, $\theta_s = 0.06$ rad, and $R = 5$.

the superscripts, stripping and direct, denoting the stripping process and the direct reaction between nucleons, and the arctan function, together with the square root of energies, are obtained from the normalization constants K_1 and K_2 .

Now, the model displays a good approximation to the experimental distributions up to 25° – 30° . The neutrons appearing at high values of θ are probably due to evaporation. In the spirit of Serber's theory, as evidenced in Ref. [18], the interaction of a high energy particle with an atomic nucleus can be thought of as taking place in two stages. In the "prompt" or "cascade" stage, individual nucleon-nucleon collisions result in the escape of some particle from the nucleus (the second process mentioned previously). Those which do not escape eventually distribute their energy throughout the whole nucleus, which is thus raised to a highly excited state and, therefore, subsequently decays by emission of low energy particles in the second stage of the reaction. Merely three type of processes which produce neutrons coexist: stripping, direct collisions between nucleons, and evaporation. In this paper, only the two first processes are accounted for. This fact, apart from the fact that it represents a limit of our formalism, explains the low yields obtained in the angular distributions for high values of θ . In the forward direction, the neutrons coming up from evaporation are evidently considered as being due to the first two distributions. Another process can compete to boost the neutron yields emitted at high θ in a small measure, and that is the disintegration in the Coulomb field.

The distributions obtained in the frame of this formalism for 50 MeV deuteron incident energy on thick Be targets are compared with experimental data in Fig. 4. For $E_n > 25$ MeV (E_n from now on will denote the energy of the neutrons for different distributions), the theory succeeds in reflecting the data in a satisfactory manner. The experimental pronounced peak at $E_d \approx 20$ MeV is attenuated in the calculations and the yields of the neutrons with energies smaller than 20 MeV are overestimated by the simulations. This behavior is due to the fact that the evaporated neutrons are considered to be emerging also from the two former processes: the stripping and direct nuclear collisions. The shape of the theoretical distribution exhibits a maximum at an energy of neutrons lower than that given by the experiment by approximately 2 MeV. A similar theoretical behavior of the energetic distributions is predicted by the calculations effected in Ref. [5]. In this reference, the maximum of the distribution is also found at a lower value than the experimental one. Also, as in our simulations, the yields of neutrons with energies lower than that of the maximum yield are overestimated. In this reference, a normalization was effected for the peak amplitude of the calculated spectrum so as to have the same value as the measured spectrum. In this circumstance, it is difficult to know the total production rate expected by

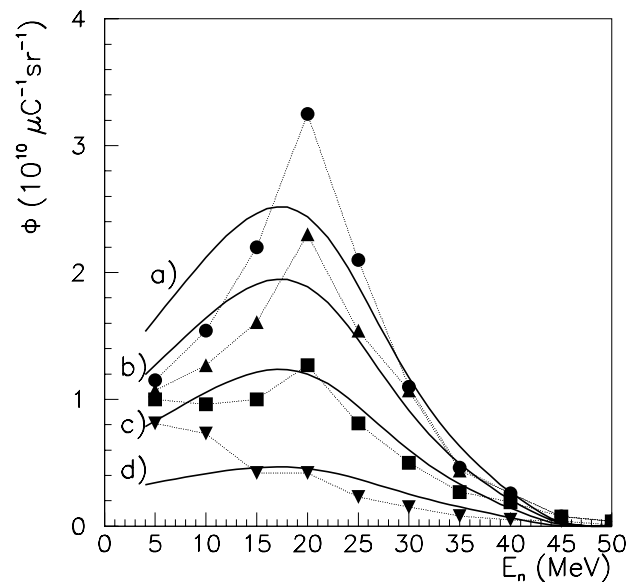


FIG. 4. Experimental energetic distributions of neutrons for 50 MeV ^2H incident energy on a thick Be target from Ref. [11]: filled circles at 0° , filled triangles with up-point at 5° , filled squares at 10° , and filled triangles with down-point at 25° . These distributions are compared with theoretical ones: (a) 0° , (b) 5° , (c) 10° , and (d) 25° . The dotted lines are to guide the eye.

the calculations. As a difference, in our simulations, the total neutron flux is approximately equal to that obtained experimentally in the limits of Serber's theory and of the semiempirical relation (22) for angles up to 20° – 25° . This characteristic favors this kind of simulation, which is easy to evaluate, for practical purposes. In this simulation, together with that from Ref. [5], an average of distributions along the range of the incident particle is taken into account. In this context, the experimental peak found at 20 MeV [$(E_d/2 - 5)$ MeV] in Fig. 3 can be due to a cross section intensification at the entrance surface of the target, because the average on the range of the particle in the target predicts a lower value (≈ 17.5 – 18 MeV).

It can be accepted that R determined previously is a function of the deuteron energy only and its values can be extrapolated for other kinds of targets. Further, to determine the cross section for other targets, it can be assumed that the major part of the neutrons is given by the stripping of the deuteron. In this case, the most important factor playing a role in the simulations for other targets is the stripping cross section. In this approximation, the following formula can be used to determine the yield at 0° for a target made from an elemental material X:

$$Y_X = Y_{\text{Be}} \frac{\int_0^{T_X(E^{\max})} \sigma(E) \frac{A_{\text{Be}}^{2/3}}{A_X^{2/3}} \frac{A_X^{1/3} + 2^{1/3}}{A_{\text{Be}}^{1/3} + 2^{1/3}} \left(1 - \frac{E_c^X}{E}\right) dt}{\int_0^{T_{\text{Be}}(E^{\max})} \sigma(E) \left(1 - \frac{E_c^{\text{Be}}}{E}\right) dt}, \quad (26)$$

where Y_X is the yield for the X target, Y_{Be} the yield for the Be target, $\sigma(E)$ is given by the formula (23), and A_X is the mass number of the X target while A_{Be} is the mass number of the Be target. The integral is effected over the range t of the ${}^2\text{He}$ in the material and thus will differ from one target to another. The differences in the integrals are given by $T(E_d)$, which is not the same for the two targets because it depends on A_X and Z_X , and by the Coulomb barrier. The ratio between the mass numbers in the first integral is deduced from two assumptions:

(i) The neutron yield is proportional to the number of atoms in the deuteron range [19]. So the range T (in mg/cm^2) must be divided by A_X .

(ii) The Serber stripping cross section is proportional to the product between $A_X^{1/3}$ of the target nucleus and $r_0(A_X^{1/3} + A_d^{1/3})$, where A_d is the deuteron mass number.

In the case of a C target, a correction is imposed by the fact that its root mean square radius is even smaller than the Be radius [20] and, therefore, does not follow the general rule $r_0A^{1/3}$. The yield of the C target must be corrected by $c = A_{Be}^{1/3}/A_C^{1/3} \times 2.5/2.47 = 0.92$ (2.5 fm is the root mean square radius of Be while 2.47 fm is that of C) in order for the formula to be valid.

From this relation, the ratio $Y_{Be}/Y_C = 1.4$ was deduced while the experimental value [19] is 1.5 (expected error $\pm 20\%$) at 54 MeV deuteron incident energy. This result contradicts the systematic presented in Ref. [17], where approximately one order of magnitude is claimed to exist between the yields expected for C and Be targets.

First, the formalism is applied to determine the distributions from a thick Be target with ${}^2\text{H}$ incident energies of 28, 20, and 17 MeV and to compare the simulations with the experimental data. The interpolated R values are, respectively, 4, 4.5, and 5, while the fluxes at 0° from formula (22) in the same succession are 1.29×10^{11} , 5.35×10^{10} , and $3.48 \times 10^{10} \mu\text{C}^{-1} \text{sr}^{-1}$.

In Fig. 5 the angular distribution simulations at 28 MeV (curve a), 20 MeV (curve b), and 17 MeV (curve c) are compared with experimental results at the same deuteron energies. The simulation reproduces the general behavior of the distributions: the maximum value is obtained at 0° , the yields are reproduced at 0° for incident deuteron energies 28 and 20 MeV in the limit of experimental errors, and the widths at half maximum are also well reproduced. Unfortunately, the curve c overestimates the neutron yields by approximately 25%, this value being greater than the experimental error of $\pm 15\%$.

In Figs. 6, 7, and 8, experimental and theoretical energetic distributions are compared in the case of the Be target for 28, 20, and 17 MeV deuteron energies, respectively. It must be specified from the beginning that the normalizations of the theoretical energetic distributions are determined from the theoretical angular distributions [calculated with the semiempirical formula (22) to obtain the yield in the forward direction of the beam and displayed

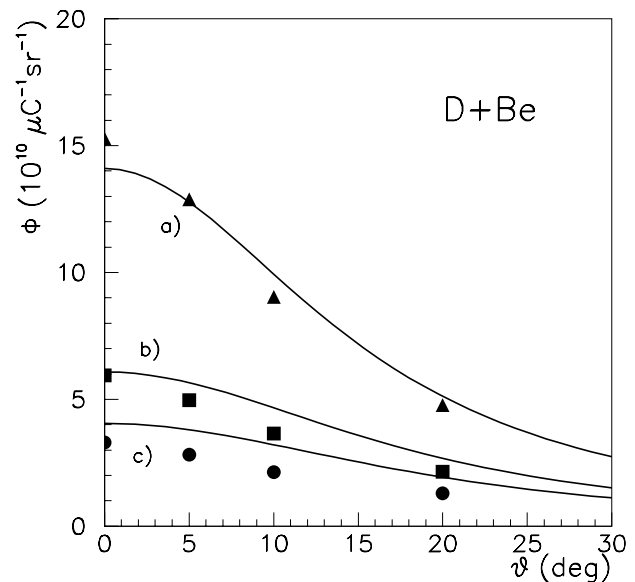


FIG. 5. Experimental angular distributions of neutrons obtained in the present experiment for $E_d = 28$ MeV (filled triangles), $E_d = 20$ MeV (filled squares), and $E_d = 17$ MeV (filled circles) for Be targets. The data are compared with simulations [full curves (a) $E_d = 28$ MeV, (b) $E_d = 20$ MeV, and (c) $E_d = 17$ MeV] at the same energies.

in Fig. 6]. Renormalizations are not effected for the theoretical curves to test the reliability of the formalism and its limits. In Fig. 6, at 0° , it is evident that the yield is underestimated because the total theoretical production was smaller than the experimental one. For the last three curves (at 5° , 10° , and 20°), the total experimental and theoretical

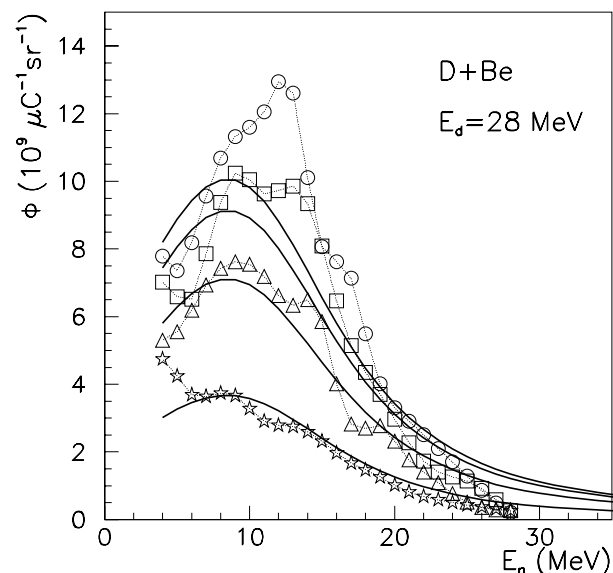


FIG. 6. Experimental energetic distributions of neutrons from Be targets obtained in the present experiment for $\theta = 0^\circ$ (circles), 5° (squares), 10° (triangles), and 20° (stars) for $E_d = 28$ MeV compared to simulations at the same energy (full curves). The dashed lines are to guide the eye.

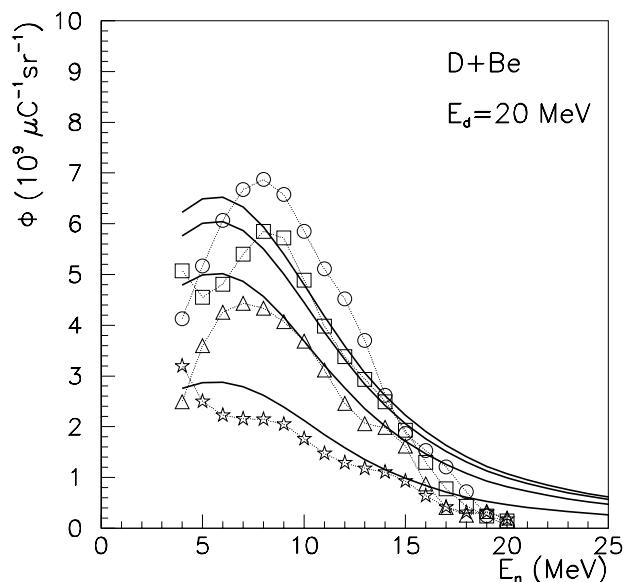


FIG. 7. Experimental energetic distributions of neutrons from Be targets for $\theta = 0^\circ$ (circles), 5° (squares), 10° (triangles), and 20° (stars) for $E_d = 20$ MeV compared to simulations at the same energy (full curves). The dashed lines are to guide the eye.

yields agree, the theory succeeding in reproducing the experimental data within experimental errors. As a general remark, the maximum of the productivities is obtained at lower neutron energies than given experimentally. The theoretical maximum is obtained at about 9 MeV while the experiment gives a peak at ≈ 10 MeV with one exception: the experimental curve at 0° gives a maximum at

12 MeV. It is interesting to note that the experimental data show a second peak at about 13 MeV for the distributions at 5° and 10° , while at 0° an attenuated peak can be discerned at 10 MeV. These peaks can be due to neutrons emerging from the kapton foil and Al envelope. In Fig. 7, the right flank of the energetic distribution is well enough reproduced (neutron energies between 13 and 20 MeV). The maximum of the theoretical productivities are again at lower energies than those found experimentally. The experimental peak is at about 8 MeV while the theoretical one is at ≈ 6.5 MeV. In Fig. 8, due to the overestimation of the total productivities when the angular distributions were calculated, the curves exceed the trends displayed by the experimental points. Again, the theoretical maximum is shifted toward lower values of the energies: the experimental peaks of the maximal yield are located about 7 MeV while 5 MeV are obtained theoretically.

In Fig. 9, the experimental angular distributions of neutrons at 28 and 20 MeV incident deuteron energies from the C target are displayed. The simulation at 0° agrees in the limit of experimental errors with the data but for both energies overestimates the experimental values by 3% and 10% for 28 and 20 MeV, respectively. Despite this discrepancy, the extrapolation (26) predicts well enough the yields for other targets and this behavior demonstrates that the assumptions (i) and (ii) used to determine this relation are valid. A similar trend, marked by an overestimation of the yields at lower incident energy, was also noticed for the Be target.

In Fig. 10, the experimental energetic distribution of neutrons from the C target at four angles are presented

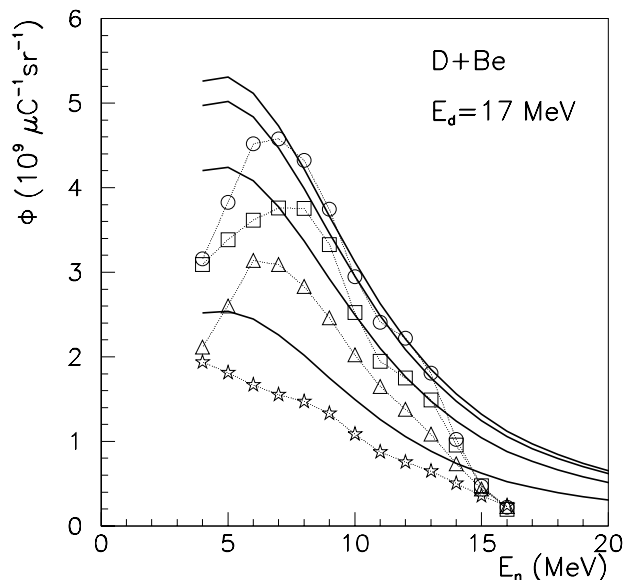


FIG. 8. Experimental energetic distributions of neutrons from Be targets for $\theta = 0^\circ$ (circles), 5° (squares), 10° (triangles) and 20° (stars) for $E_d = 17$ MeV compared to simulations at the same energy (full curves). The dashed lines are to guide the eye.

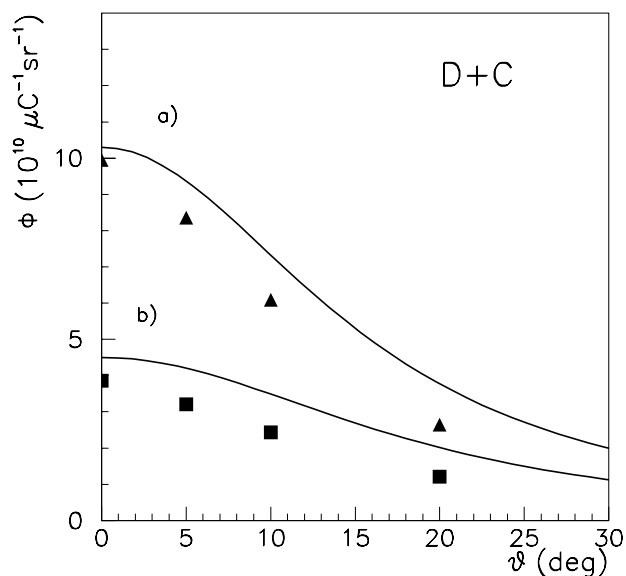


FIG. 9. Experimental angular distributions of neutrons obtained in the present experiment for $E_d = 28$ MeV (filled triangles) and $E_d = 20$ MeV (filled squares) for C targets. The data are compared with simulations [full curves (a) $E_d = 28$ MeV and (b) $E_d = 20$ MeV] at the same energies.

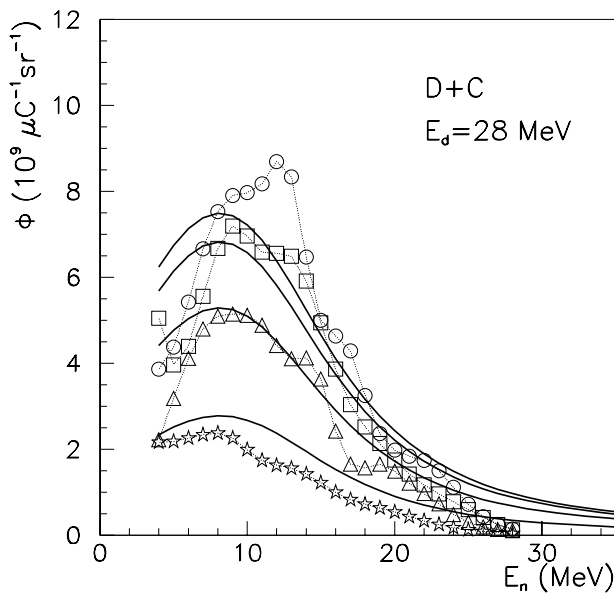


FIG. 10. Experimental energetic distributions from the C target for $\theta = 0^\circ$ (circles), 5° (squares), 10° (triangles) and 20° (stars) for $E_d = 28$ MeV compared to simulations at the same energy (full curves). The dashed lines are to guide the eye.

for $E_d = 28$ MeV. Comparisons with the simulations show that, again, the maximum of the yield is predicted at a lower energy. Apart from this fact, the theoretical curves succeed in reproducing correctly the experimental points. In the case of $E_d = 20$ MeV, the experimental data for the C target are plotted in Fig. 11. Apart from the systematically lower yields, the behavior of the

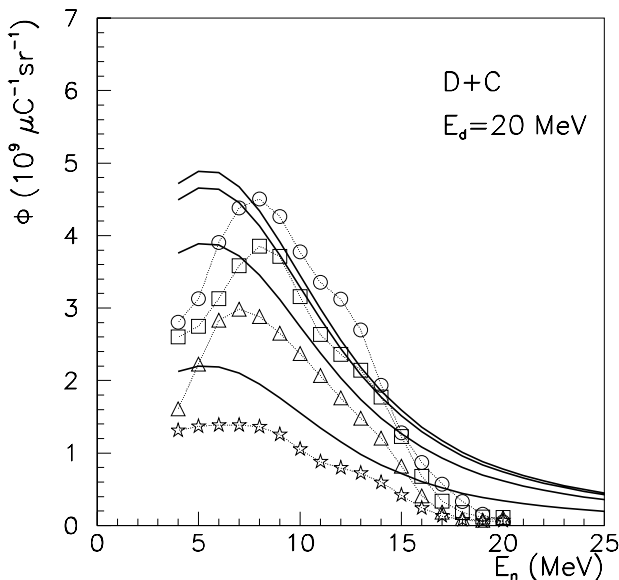


FIG. 11. Experimental energetic distributions from the C target for $\theta = 0^\circ$ (circles), 5° (squares), 10° (triangles), and 20° (stars) for $E_d = 20$ MeV compared to simulations at the same energy (full curves).

experimental data from C is very similar to that of the Be converter.

In Fig. 12, the angular distribution of neutrons delivered by the U target are presented for the deuteron incident energies of 28 and 20 MeV. The theory fails to reproduce correctly the shape of the distribution, the parametrization giving a wider angular spread than what is experimentally determined. At the same time, it can be observed that the yields at 0° are well predicted by the formula (26) if we acknowledge the fact that the U target presents physical properties very different from that of the Be one, used as reference. It is of interest to note that, this time, the yield at 28 MeV incident energy of deuterons is overestimated, while at 20 MeV it is underestimated. In Fig. 13, the experimental energetic distributions at four angles are plotted. Peaks for the maximum productivities observed at 0° , 5° , and 10° are not predicted by the simulations. Only two curves were drawn for the simulations: one at 0° (because the curves for 0° , 5° , and 10° are similar) and one for 20° . The right flank of the experimental distribution at 0° is well described by the trend of the theoretical curve. Finally, in Fig. 14, the energetic distributions delivered by the U target are presented for $E_d = 20$ MeV. The shapes of the distributions are governed by a wide peak at about 10 MeV characterized by some fluctuations. The position of the maximum of the peak and the width at half maximum agree with the values obtained for stripping (theoretically the peak at 10 MeV and the width at half maximum of 9 MeV can be obtained in the frame of Serber's theory), and these

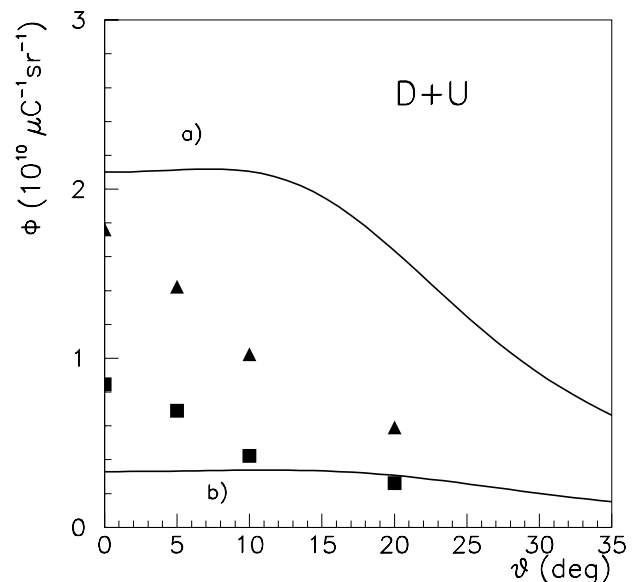


FIG. 12. Experimental angular distributions of neutrons obtained in the present experiment for $E_d = 28$ MeV (filled triangles) and for $E_d = 20$ MeV (filled squares) for U targets. The data are compared with simulations [full curves (a) $E_d = 28$ MeV and (b) $E_d = 20$ MeV] at the same energies. The dashed lines are to guide the eye.

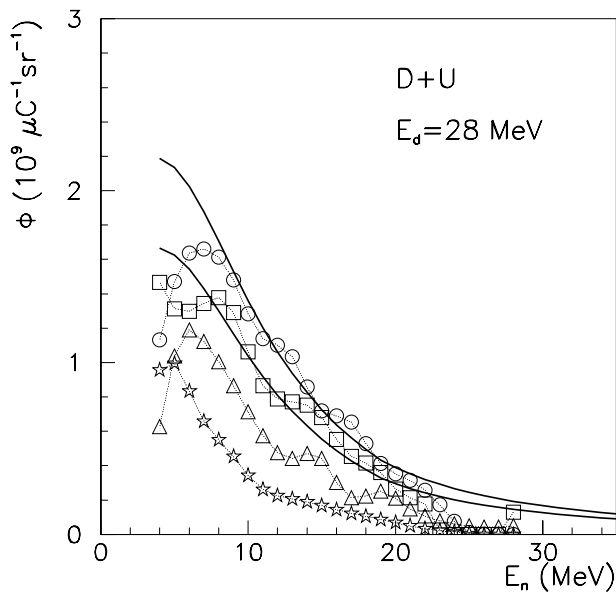


FIG. 13. Experimental energetic distributions of neutrons from the U target for $\theta = 0^\circ$ (circles), 5° (squares), 10° (triangle), and 20° (stars) for $E_d = 28$ MeV compared to simulations at the same energy (full curves). The upper curve is the theoretical distribution at 0° while the second one corresponds to 20° . The dashed lines are to guide the eye.

nucleons can be due to the kapton window and the Al envelope. It is also possible that these behaviors are determined by neutrons emitted in fission processes. These phenomena are not tractable in the case of our formalism. These neutrons emitted by the kapton window, the Al en-

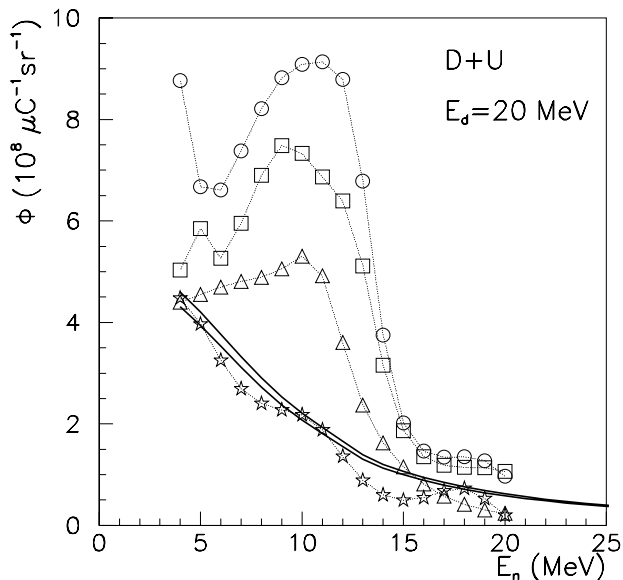


FIG. 14. Experimental energetic distributions of neutrons from the U target for $\theta = 0^\circ$ (circles), 5° (squares), 10° (triangles), and 20° (stars) for $E_d = 20$ MeV compared to simulations at the same energy (full curves). The upper curve is the theoretical distribution at 0° while the second one corresponds to 20° . The dashed lines are to guide the eye.

velope, and the fission residues may interfere with those given by the U target and can cause greater yields than those given by our semiempirical parametrization.

V. CONCLUSIONS

The neutron yields are determined only up to 20° because this angular width is pertinent to our R&D program. This type of simulation provides a useful tool for the optimization of the geometries of the (Be, C, or U) converter- ^{238}U fission source unit in order to yield the best productions of neutron-rich elements. In spite of its lower neutron yields compared to that given by the Be, the C converter becomes more suitable for our applications because it can be displayed very close to the ^{238}U isotope source (therefore the corresponding solid angle is greater), thus reducing transuranic element contaminations. The Be has a lower melting temperature than C; therefore, the Be converter must be positioned at a greater distance from the source, must be cooled, and, also, presents health hazards that C does not. Calculations were already performed [21] with different distributions of the neutron flux and different geometries of our system, proving the superiority of the C converter for our goal. Parallel to this work, the advantages of C have been experimentally evidenced [22] when measuring neutron rich exotic nuclei production in the same deuteron energy range.

ACKNOWLEDGMENTS

The authors thank Professor S. Galès, Professor P. Roussel, and Professor R. Bimbot for illuminating discussions and support. This work was sponsored by the European Contract SPRAIL II No. ERB 4062 PL 975009 and by IN2P3 No. FMGE CT 980100.

APPENDIX: ANGULAR DISTRIBUTION CALCULATION

The Δ operator and its powers are

$$\begin{aligned} \Delta &= \frac{1}{\xi} \frac{\partial}{\partial \xi} + \frac{\partial^2}{\partial \xi^2}, \\ \Delta^2 &= \frac{1}{\xi^3} \frac{\partial}{\partial \xi} - \frac{1}{\xi^2} \frac{\partial^2}{\partial \xi^2} + \frac{2}{\xi} \frac{\partial^3}{\partial \xi^3} + \frac{\partial^4}{\xi^4}, \\ \Delta^3 &= \frac{9}{\xi^5} \frac{\partial}{\partial \xi} - \frac{9}{\xi^4} \frac{\partial^2}{\partial \xi^2} + \frac{6}{\xi^3} \frac{\partial^3}{\partial \xi^3} - \frac{3}{\xi^2} \frac{\partial^4}{\partial \xi^4} \\ &\quad + \frac{3}{\xi} \frac{\partial^5}{\partial \xi^5} + \frac{\partial^6}{\partial \xi^6}. \end{aligned} \quad (\text{A1})$$

The product given by Eq. (3) can be put in the following form after some simple operations:

$$GP(\xi) = \frac{1}{2\pi} \left\{ P(\xi) + \frac{\xi_s^2}{8\xi} \frac{\partial P(\xi)}{\partial \xi} + \frac{\xi_s^4}{96\xi^2} \left(\frac{1}{\xi} \frac{\partial P(\xi)}{\partial \xi} - \frac{\partial^2 P(\xi)}{\partial \xi^2} \right) + \frac{\xi_s^2}{8} \frac{\partial^2 P(\xi)}{\partial \xi^2} + \frac{2\xi_s^4}{96\xi} \frac{\partial^3 P(\xi)}{\partial \xi^3} + \frac{\xi_s^4}{96} \frac{\partial^4 P(\xi)}{\partial \xi^4} \right. \\ \left. + \frac{\xi_s^6}{864} \left[\frac{9}{\xi^5} \frac{\partial}{\partial \xi} - \frac{9}{\xi^4} \frac{\partial^2}{\partial \xi^2} + \frac{6}{\xi^3} \frac{\partial^3}{\partial \xi^3} - \frac{3}{\xi^2} \frac{\partial^4}{\partial \xi^4} + \frac{3}{\xi} \frac{\partial^5}{\partial \xi^5} \right] P(\xi) + \frac{\xi_s^6}{864} \frac{\partial^6}{\partial \xi^6} P(\xi) \right\}, \quad (A2)$$

where

$$P(\xi) = \frac{f[u(\xi)]}{p(\xi)^{3/2}}, \quad (A3)$$

with

$$f[u(\xi)] = u^{3/2}(\xi)P_{1/2}[u(\xi)], \quad p(\xi) = (1 + \xi^2 + \xi_c^2), \quad (A4)$$

and the partial derivatives

$$\frac{\partial P[u(\xi)]}{\partial \xi} = \frac{\frac{\partial f}{\partial u} u'}{p^{3/2}} - \frac{3f\xi}{p^{5/2}}, \quad (A5)$$

$$\frac{\partial^2 P[u(\xi)]}{\partial \xi^2} = \frac{\frac{\partial^2 f}{\partial u^2} (u')^2 + \frac{\partial f}{\partial u} u''}{p^{3/2}} - \frac{6\frac{\partial f}{\partial u} u' \xi + 3f(u)}{p^{5/2}} + \frac{15f(u)\xi^2}{p^{7/2}}, \quad (A6)$$

$$\frac{\partial^3 P[u(\xi)]}{\partial \xi^3} = \frac{\frac{\partial^3 f}{\partial u^3} (u')^3 + 3\frac{\partial^2 f}{\partial u^2} u' u'' + \frac{\partial f}{\partial u} u'''}{p^{3/2}} - 9\frac{\frac{\partial^2 f}{\partial u^2} (u')^2 \xi + \frac{\partial f}{\partial u} u'' \xi + \frac{\partial f}{\partial u} u'}{p^{5/2}} + 45\frac{\frac{\partial f}{\partial u} u' \xi^2 + f\xi}{p^{7/2}} - 105f\xi^3 p^{9/2}, \quad (A7)$$

$$\frac{\partial^4 P[u(\xi)]}{\partial \xi^4} = \frac{\frac{\partial^4 f}{\partial u^4} (u')^4 + 6\frac{\partial^3 f}{\partial u^3} (u')^2 u'' + 3\frac{\partial^2 f}{\partial u^2} (u'')^2 + 4\frac{\partial^2 f}{\partial u^2} u' u'''}{p^{3/2}} \\ - 6\frac{2\frac{\partial^3 f}{\partial u^3} (u')^3 \xi + 6\frac{\partial^2 f}{\partial u^2} u' u'' \xi + 2\frac{\partial f}{\partial u} u'''}{p^{5/2}} + 45\frac{2\frac{\partial^2 f}{\partial u^2} (u')^2 \xi^2 + 2\frac{\partial f}{\partial u} u'' \xi^2 + 4\frac{\partial f}{\partial u} u' \xi + f}{p^{7/2}} - 10\frac{42\frac{\partial f}{\partial u} u' \xi^3 + 63f\xi^2}{p^{9/2}} + 945\frac{f\xi^4}{p^{11/2}}, \quad (A8)$$

$$\frac{\partial^5 P[u(\xi)]}{\partial \xi^5} = \left\{ \frac{\partial^5 f}{\partial u^5} (u')^5 + 10\frac{\partial^4 f}{\partial u^4} (u')^3 u'' + 15\frac{\partial^3 f}{\partial u^3} u' (u'')^2 + 10\frac{\partial^3 f}{\partial u^3} (u')^2 u'''} \right. \\ \left. + 10\frac{\partial^2 f}{\partial u^2} u'' u'''} + \frac{\partial^2 f}{\partial u^2} u' u^{IV} + \frac{\partial f}{\partial u} u^V \right\} \frac{1}{p^{3/2}} \\ - \left\{ 15\frac{\partial^4 f}{\partial u^4} (u')^4 \xi + 90\frac{\partial^3 f}{\partial u^3} (u')^2 u'' \xi + 30\frac{\partial^3 f}{\partial u^3} (u')^3 + 45\frac{\partial^2 f}{\partial u^2} (u'')^2 \xi \right. \\ \left. + 24\frac{\partial^2 f}{\partial u^2} u' u'' \xi + 90\frac{\partial^2 f}{\partial u^2} u' u'' + 15\frac{\partial f}{\partial u} u^{IV} \xi + 30\frac{\partial f}{\partial u} u'' \right\} \frac{1}{p^{5/2}} \\ + \left\{ 150\frac{\partial^3 f}{\partial u^3} (u')^3 \xi^2 + 450\frac{\partial^2 f}{\partial u^2} u' u'' \xi^2 + 450\frac{\partial^2 f}{\partial u^2} (u')^2 \xi \right. \\ \left. + 150\frac{\partial f}{\partial u} u'' \xi^2 + 450\frac{\partial f}{\partial u} u'' \xi + 225\frac{\partial f}{\partial u} u' \right\} \frac{1}{p^{7/2}} \\ - \left\{ 1050\frac{\partial^2 f}{\partial u^2} (u')^2 \xi^3 + 1050\frac{\partial f}{\partial u} u'' \xi^3 + 2950\frac{\partial f}{\partial u} u' \xi^2 + 1575f\xi \right\} \frac{1}{p^{9/2}} \\ + \left\{ 4725\frac{\partial f}{\partial u} u' \xi^4 + 9450f\xi^3 \right\} \frac{1}{p^{11/2}} - 10395\frac{f\xi^5}{p^{13/2}}, \quad (A9)$$

$$\begin{aligned}
\frac{\partial^6 P[u(\xi)]}{\partial \xi^6} = & \left\{ \frac{\partial^6 f}{\partial u^6} (u')^6 + 15 \frac{\partial^5 f}{\partial u^5} (u')^4 u'' + 45 \frac{\partial^4 f}{\partial u^4} (u')^2 (u'')^2 + 20 \frac{\partial^4 f}{\partial u^4} (u')^3 u''' + 15 \frac{\partial^3 f}{\partial u^3} (u'')^3 + 60 \frac{\partial^3 f}{\partial u^3} u' u'' u''' \right. \\
& + 11 \frac{\partial^3 f}{\partial u^3} (u')^2 u^{IV} + 10 \frac{\partial^2 f}{\partial u^2} (u''')^2 + 11 \frac{\partial^2 f}{\partial u^2} u'' u^{IV} + 2 \frac{\partial^2 f}{\partial u^2} u' u^V + \left. \frac{\partial f}{\partial u} u^{VI} \right\} \frac{1}{p^{3/2}} \\
& - \left\{ 18 \frac{\partial^5 f}{\partial u^5} (u')^5 \xi + 180 \frac{\partial^4 f}{\partial u^4} (u')^3 u'' \xi + 270 \frac{\partial^3 f}{\partial u^3} u' (u'')^2 \xi + 144 \frac{\partial^3 f}{\partial u^3} (u')^2 u''' \xi + 144 \frac{\partial^2 f}{\partial u^2} u'' u''' \xi \right. \\
& + 42 \frac{\partial^2 f}{\partial u^2} u' u^{IV} \xi + 16 \frac{\partial f}{\partial u} u^V \xi + 45 \frac{\partial^4 f}{\partial u^4} (u')^4 + 270 \frac{\partial^3 f}{\partial u^3} u'^2 u'' \\
& + 135 \frac{\partial^2 f}{\partial u^2} (u'')^2 + 144 \frac{\partial^2 f}{\partial u^2} u' u''' + \left. 45 \frac{\partial f}{\partial u} u^{IV} \right\} \frac{1}{p^{5/2}} \\
& + \left\{ 195 \frac{\partial^4 f}{\partial u^4} (u')^4 \xi^2 + 1350 \frac{\partial^3 f}{\partial u^3} (u')^2 u'' \xi^2 + 900 \frac{\partial^3 f}{\partial u^3} (u')^3 \xi + 675 \frac{\partial^2 f}{\partial u^2} (u'')^2 \xi^2 \right. \\
& + 270 \frac{\partial^2 f}{\partial u^2} u' u''' \xi^2 + 2250 \frac{\partial^2 f}{\partial u^2} u' u'' \xi + 195 \frac{\partial f}{\partial u} u^{IV} \xi^2 + 900 \frac{\partial f}{\partial u} u''' \xi + 675 \frac{\partial^2 f}{\partial u^2} (u')^2 \\
& + 450 \frac{\partial f}{\partial u} u'' + 500 \frac{\partial^2 f}{\partial u^2} (u')^2 \left. \right\} \frac{1}{p^{7/2}} \\
& - \left\{ 2250 \frac{\partial^3 f}{\partial u^3} (u')^3 \xi^3 + 6750 \frac{\partial^2 f}{\partial u^2} u' u'' \xi^3 + 9700 \frac{\partial^2 f}{\partial u^2} (u')^2 \xi^2 + 2250 \frac{\partial f}{\partial u} u''' \xi^3 \right. \\
& + 7800 \frac{\partial f}{\partial u} u'' \xi^2 + 4275 \frac{\partial f}{\partial u} u' + 1575 f \left. \right\} \frac{1}{p^{9/2}} \\
& + \left\{ 14\,175 \frac{\partial^2 f}{\partial u^2} (u')^2 \xi^4 + 14\,175 \frac{\partial f}{\partial u} u'' \xi^4 + 46\,900 \frac{\partial f}{\partial u} u' \xi^2 + 42\,525 f \xi^2 \right\} \frac{1}{p^{11/2}} \\
& - \left\{ 71\,820 \frac{\partial f}{\partial u} u' \xi^5 + 174\,825 f \xi^4 \right\} \frac{1}{p^{13/2}} + \frac{1\,305\,135 f \xi^6}{p^{15/2}}. \tag{A10}
\end{aligned}$$

In these equalities, we can approximate

$$P_{1/2}(u) = 1 + \frac{3}{4} \frac{u-1}{2} - \frac{15}{64} \left(\frac{u-1}{2} \right)^2 + \frac{35}{256} \left(\frac{u-1}{2} \right)^3, \tag{A11}$$

so that

$$\frac{\partial f}{\partial u} = \frac{3}{2} u^{1/2} P_{1/2}(u) + u^{3/2} B(u), \tag{A12}$$

$$\frac{\partial^2 f}{\partial u^2} = \frac{3}{4} u^{-1/2} P_{1/2}(u) + 3u^{1/2} B(u) + u^{3/2} C(u), \tag{A13}$$

$$\frac{\partial^3 f}{\partial u^3} = -\frac{3}{8} u^{-3/2} P_{1/2}(u) + \frac{9}{4} u^{-1/2} B(u) + \frac{9}{2} u^{1/2} C(u) + u^{3/2} D(u), \tag{A14}$$

$$\frac{\partial^4 f}{\partial u^4} = \frac{9}{16} u^{-5/2} P_{1/2}(u) - \frac{6}{4} u^{-3/2} B(u) + \frac{9}{2} u^{-1/2} C(u) + 6u^{1/2} D(u), \tag{A15}$$

$$\frac{\partial^5 f}{\partial u^5} = -\frac{45}{32} u^{-7/2} P_{1/2}(u) + \frac{27}{16} u^{-5/2} B(u) - \frac{15}{4} u^{-3/2} C(u) + \frac{15}{2} u^{-1/2} D(u), \tag{A16}$$

$$\frac{\partial^6 f}{\partial u^6} = \frac{315}{64} u^{-9/2} P_{1/2}(u) - \frac{180}{32} u^{-7/2} B(u) + \frac{117}{16} u^{-5/2} C(u) - \frac{15}{2} u^{-3/2} D(u), \quad (\text{A17})$$

$$B(u) = \frac{3}{8} - \frac{15}{64} \frac{u-1}{2} + \frac{105}{512} \left(\frac{u-1}{2} \right)^2, \quad (\text{A18})$$

$$C(u) = -\frac{15}{128} + \frac{105}{512} \frac{u-1}{2}, \quad (\text{A19})$$

$$D(u) = \frac{105}{1024}, \quad (\text{A20})$$

$$\frac{\partial u}{\partial \xi} = \frac{2\xi}{g^{1/2}} - \frac{1}{2} \frac{hg'}{g^{3/2}}, \quad (\text{A21})$$

$$\frac{\partial^2 u}{\partial \xi^2} = \frac{2}{g^{1/2}} - \frac{1}{2} \frac{4\xi g' + hg''}{g^{3/2}} + \frac{3}{4} \frac{h(g')^2}{g^{5/2}}, \quad (\text{A22})$$

$$\frac{\partial^3 u}{\partial \xi^3} = -\frac{3g' + 3g''\xi + 12h\xi}{g^{3/2}} + \frac{9}{4} \frac{2(g')^2\xi + hg'g''}{g^{5/2}} - \frac{15}{8} \frac{h(g')^3}{g^{7/2}}, \quad (\text{A23})$$

$$\begin{aligned} \frac{\partial^4 u}{\partial \xi^4} = & -\frac{6g'' + 96\xi^2 + 12h}{g^{3/2}} + \frac{9(g')^2 + 18g'g''\xi + 72hg'\xi + \frac{9}{4}h(g'')^2}{g^{5/2}} \\ & - \frac{15(g')^3\xi + \frac{45}{4}h(g')^2g''}{g^{7/2}} + \frac{105}{16} \frac{hg''}{g^{9/2}}, \end{aligned} \quad (\text{A24})$$

$$\begin{aligned} \frac{\partial^5 u}{\partial \xi^5} = & -360 \frac{\xi}{g^{3/2}} + \frac{45g'g'' + 720g'\xi^2 + 90hg' + \frac{45}{2}(g'')^2\xi + 180hg''\xi}{g^{5/2}} \\ & - \frac{\frac{75}{2}(g')^3 + \frac{195}{2}(g')^2g''\xi + 450h(g')^2\xi + \frac{225}{8}hg'(g'')^2}{g^{7/2}} + \frac{\frac{525}{8}(g')^4\xi + \frac{525}{8}h(g')^3g''}{g^{9/2}} - \frac{945}{32} \frac{h(g')^5}{g^{11/2}}, \end{aligned} \quad (\text{A25})$$

$$\begin{aligned} \frac{\partial^6 u}{\partial \xi^6} = & -\frac{360}{g^{3/2}} + \frac{5400g'\xi + \frac{135}{2}(g'')^2 + 90hg'' + 4320h\xi^2}{g^{5/2}} \\ & - \frac{225(g')^2g'' + \frac{615}{2}g'(g'')^2\xi + 5040(g')^2\xi^2 + 2600hg'g''\xi}{g^{7/2}} + \frac{675h(g')^2 + \frac{225}{8}h(g'')^3}{g^{7/2}} \\ & + \frac{\frac{2625}{8}(g')^4 + 735(g')^3g''\xi + 3150h(g')^3\xi + \frac{4725}{16}h(g')^2(g'')^2}{g^{9/2}} \\ & - \frac{\frac{2835}{8}(g')^5\xi + \frac{8035}{16}h(g')^4g''}{g^{11/2}} + 10395 \frac{h(g')^6}{g^{13/2}}, \end{aligned} \quad (\text{A26})$$

$$h(\xi) = 1 + \xi^2 + \xi_c^2, \quad (\text{A27})$$

$$g(\xi) = (1 + \xi^2 + \xi_c^2)^2 - 4\xi^2\xi_c^2, \quad (\text{A28})$$

$$g'(\xi) = 4(1 + \xi^2 + \xi_c^2)\xi - 8\xi\xi_c^2, \quad (\text{A29})$$

$$g''(\xi) = 4 + 12\xi^2 - 4\xi_c^2. \quad (\text{A30})$$

These formulas are also valid for $\theta = 0$. In the case of $\theta = 0$, at first view, some singularities in the origin

of Eq. (A2) due to the division by ξ , ξ^3 , and ξ^5 of the partial derivative $\partial P/\partial \xi$, the division by ξ^2 and ξ^4 of the partial derivative $\partial^2 P/\partial \xi^2$, and the division by ξ^3 of $\partial^3 P/\partial \xi^3$ can occur. These uncertainties can be immediately removed by taking into account that all the terms in the expression $\partial P/\partial \xi$ can be factorized by ξ , the terms in the expression $\partial^2 P/\partial \xi^2$ can be factorized by ξ^2 , and so on. Moreover, the expression in parentheses from

Eq. (A2),

$$\frac{1}{\xi} \frac{\partial P}{\partial \xi} - \frac{\partial^2 P}{\partial \xi^2} = \frac{\frac{\partial f}{\partial u} \left[\xi \frac{3g' + 4h\xi}{g^{3/2}} - \frac{3}{4} \frac{hg'}{g^{5/2}} \right] - \frac{\partial^2 f}{\partial u^2} (u')^2}{p^{3/2}} + 6 \frac{\frac{\partial f}{\partial u} u' \xi}{p^{5/2}} - 15 \frac{f \xi^2}{p^{7/2}}, \quad (\text{A31})$$

is not singular in 0. Moreover, the limit for $\xi \rightarrow 0$ of the expression given by the action of the sum of the operators in the square bracket on the right-hand side of Eq. (A2) on P is 0. The resulting detailed formulas are not displayed to avoid useless complications of this appendix.

-
- [1] J. A. Nolen, in *Radioactive Nuclear Beams*, edited by D. J. Morrissey (Editions Frontières, Gif-sur-Yvette, 1993), p. 111.
- [2] F. Clapier, A. Mueller, C. Obert, O. Bajeat, M. Ducourtieux, A. Ferro, A. Horbowa, L. Kotfila, C. Lau, H. Lefort, S. Kandry-Rody, N. Pauwels, J. C. Poitier, J. Proust, J. C. Putaux, C. F. Liang, P. Paris, A. C. C. Villari, R. Lichtenhaler, L. Maunoury, and J. Lettry, *Phys. Rev. ST Accel. Beams* **1**, 013501 (1998).
- [3] M. Mirea, F. Clapier, N. Pauwels, and J. Proust, *Nuovo Cimento* **111A**, 267 (1998).
- [4] R. Serber, *Phys. Rev.* **72**, 1008 (1947).
- [5] R. Madey, F. M. Waterman, and A. R. Baldwin, *Phys. Rev. C* **14**, 801 (1976).
- [6] D. Christenson, M. W. McNaughton, and J. A. Jungerman, *Nucl. Instrum. Methods* **160**, 499 (1979).
- [7] A. Belyman, A. Hoummada, J. Collot, P. de Saintignon, G. Mahout, and B. Merkel, *Nucl. Instrum. Methods Phys. Res., Sect. B* **134**, 217 (1998).
- [8] S. Cierjacks, Y. Hino, F. Raupp, L. Buth, D. Filges, P. Cloth, and T. W. Armstrong, *Phys. Rev. C* **36**, 1976 (1987).
- [9] I. Tilquin, Y. El. Masri, M. Parlog, Ph. Collon, M. Hadri, Th. Keutgen, J. Lehmann, P. Deleux, P. Lipnik, A. Ninane, F. Hanappe, G. Bizard, D. Durand, P. Mosrin, J. Peter, R. Regimbart, and B. Tamain, *Nucl. Instrum. Methods Phys. Res., Sect. A* **365**, 446 (1995).
- [10] A. C. Helmholz, E. M. McMillan, and D. C. Sewell, *Phys. Rev.* **72**, 1003 (1947).
- [11] J. P. Meulders, P. Leleux, P. C. Macq, and C. Pirart, *Phys. Med. Biol.* **20**, 135 (1975).
- [12] K. Goebel and A. J. Miller, *Nucl. Instrum. Methods* **96**, 581 (1971).
- [13] G. Moliere, *Z. Naturforsch* **3A**, 78 (1947); **10A**, 177 (1955).
- [14] H. Bichsel, Preprint USC-136-150, 1970.
- [15] M. A. Lone, A. J. Ferguson, and B. C. Roberston, *Nucl. Instrum. Methods Phys. Res.* **189**, 515 (1981).
- [16] H. J. Brede, G. Dietze, K. Kudo, U. J. Schrewe, F. Tancu, and C. Wen, *Nucl. Instrum. Methods Phys. Res., Sect. A* **274**, 332 (1989).
- [17] J. A. Stokes, L. A. Parks, C. A. Preskitt, and J. John, *IEEE Trans. Nucl. Sci.* **30**, 1623 (1983).
- [18] D. M. Skyrme, *Nucl. Phys.* **35**, 177 (1962).
- [19] G. W. Schweimer, *Nucl. Phys.* **A100**, 537 (1967).
- [20] H. de Vries, C. W. de Jager, and C. de Vries, *At. Data Nucl. Data. Tables* **36**, 495 (1987).
- [21] O. Bajeat, M. Mirea, and F. Clapier, Preprint IPNO 98-03, 1998.
- [22] F. Clapier, in *Proceedings of the Fourth Specialists' Meeting on Shielding Aspects of Accelerators, Targets and Irradiation Facilities (SATIF-4)*, Knoxville, Tennessee, 1998 (to be published).